Journal of Solar Energy Research (JSER)

Journal homepage: www.jser.ut.ac.ir

Design and Analysis of LCL-type Grid-Connected PV Power Conditioning System Based on Positive Virtual Impedance Capacitor-Current Feedback Active Damping

Majid Hosseinpour[a,*], Amin Kholousi[a]

[a]*Department of Electrical Engineering, University of Mohaghegh Ardabili, Ardabil, Iran*

ARTICLE INFO

Article Type:

Research Article

Received:25.03.2023
Accepted:22.05.2023

Keywords:
LCL filter
Active damping
PV Power System
Grid-connected inverter
Solar array

A B S T R A C T

In recent years, grid-connected solar systems have become increasingly common on low-voltage grids to promote renewable energy sources. In these systems, LCL filters are commonly used to eliminate high-frequency harmonics produced by switching grid-connected inverters. However, the resonance frequency of LCL filters is highly dependent on network impedance. Variations in network impedance can shift the resonance frequency, causing instability in the system. To address this issue, this paper proposes a new method for attenuating resonance using capacitor-current feedback with positive virtual impedance shaping. It can provide a positive equivalent resistance almost within the Nyquist frequency, i.e., the entire controllable frequency range. The proposed method maintains system stability against changes in network impedance and offers good performance against changes in the production capacity of the solar array. For maximum power point tracking, the incremental conductance method and integral regulator are used. Simulation results using MATLAB/Simulink software demonstrate the effectiveness of the proposed method in injecting high-quality current into the network and maintaining stability against changes in network impedance. The proposed method can lead to improved power quality and increased efficiency of grid-connected solar systems, which can help to promote the adoption of renewable energy sources and reduce carbon emissions.

1. Introduction

Over the past few years, the excessive consumption of fossil fuels and the process of industrialization have resulted in elevated levels of carbon emissions, leading to climate change and global warming. As a result, renewable energy sources such as solar energy and wind turbines are gaining popularity and rapidly evolving [1]. Solar

*Corresponding Author Email: hoseinpour.majid@uma.ac.ir

Cite this article: Hosseinpour, M., & Kholousi, A. (2023). Design and Analysis of LCL-type Grid-Connected PV Power Conditioning System Based on Positive Virtual Impedance Capacitor-Current Feedback Active Damping. Journal of Solar Energy Research, 8(2), 1497-1515

DOI: 10.22059/jser.2023.357089.1286 DOR: 20.1001.1.25883097.2023.8.2.12.0

energy conversion systems produce a lower voltage than

the grid voltage, which necessitates increasing the voltage to match the grid voltage for grid connection. Depending on the voltage and current values of a PV module, it can produce a maximum amount of power. PV operating conditions constantly change with radiation intensity and temperature changes, so the instantaneous voltage is variable. Controlled power converters like DC-DC converters are employed to execute maximum power point tracking (MPPT) [2]. Perturb and observation (P&O) and incremental conductance (IC) methods are the most well-known MPPT methods. The incremental conductance method provides a better response than other methods for severe changes in weather conditions [3-4].

Employing grid-connected inverters in the distribution network is a practical solution for solar energy conversion systems [5]. Grid-connected inverters have some advantages, but they can also generate high-frequency harmonics. LCL filters effectively eliminate high-frequency harmonics caused by switching on inverters connected to the network. Compared to L filters, LCL filters have lower inductance, higher power density, and greater performance [6-7]. Mazaheri et al. [8] presented a simulation-aided design for LCL filters in grid-interactive PV inverters, reducing inductor size for reduced Electromagnetic Interference (EMI). Analytical and simulation constraints are used to obtain appropriate filter parameters with Total Harmonic Distortion (THD) below 5%. The resonance and sensitivity to network impedance are two critical challenges faced when using LCL filters with weak networks. Resonance due to LCL filters causes instability of the grid-tied inverter. Besides the factors already stated, control delays due to PWM reference changes and zero-order hold may also cause instability in the grid-connected inverters [9-11]. Grid-connected inverters are at risk of instability when LCL filters are used, so resonance-damping methods must be employed.

In general, resonance damping methods due to LCL filters are divided into two categories: active damping (AD) methods [12-13] and passive damping methods [14]. Compared to passive damping methods, AD methods have attracted more attention due to lower power losses, higher efficiency, and flexibility. Active damping methods include capacitor current feedback [15], capacitor voltage feedback [16], LC-trap voltage, or current feedback [17]. Yang et al. [18] proposed an improved capacitor voltage full feedforward control strategy for LCL-type grid-connected inverters based on delay compensation, which reduces the negative influence of digital control delay and improves the robustness of the system under weak grid conditions. Zhong et al. [19] suggested coordinated control of active disturbance rejection through grid voltage feedforward to achieve less than 5% THD of the injected current, meeting the grid connection standard. The capacitor current feedback-based AD method is one of the common methods for resonance damping of LCL filters [20-22]. In this method, the capacitor current feedback is considered as an impedance that is parallel to the filter capacitor. Pan et al. [23] explained that capacitor current feedback (CCF) can be regarded as a virtual impedance that creates damping using digital control and considering controlling delays. If the resonant frequency (f_{res}) of the filter is greater than one-sixth of the sampling frequency (f_{sam}) ($f_{res}>f_{sam}/6$), the virtual impedance acts as a negative resistor that causes the right Half-plane poles (RHP). It leads to a non-minimum phase behavior, as Wang et al. exhibited in [24] and [25]. As Li et al. [26] and Chen et al. [27] concluded, a more precise estimation of the gain margin is necessary to stabilize the system and avoid the formation of right poles. The gain margin requirements for resonance frequency close to $f_{sam}/6$ are hardly achievable. According to Pan et al. [28], when $f_{res}=f_{sam}/6$, the worst case is reached, making grid-connected inverters unstable. According to Huang and Rajashekara [29], and Zhao et al. [30], to meet stringent gain margin requirements, it is possible to utilize a positive equivalent resistor which leads to a minimum phase response over a wide frequency range. The frequency range of positive equivalent resistance may be extended by developing methods as suggested by Hosseinpour et al. [31] and Rasekh et al. [32] for reducing control delays or as explored by Li et al. [33], for compensating control delays.

This paper introduces an LCL filter-based grid-connected power optimizer capable of transferring solar array power to a low-voltage grid. This system utilizes a boost converter to increase the voltage produced by PV and to inject power into the grid-connected inverter DC link. To track the maximum power point, the incremental conductance method plus the integral regulator is utilized to minimize the $\frac{dI}{dV}+\frac{I}{V}$ error. For resonance damping, the AD method has been used based on capacitor-current proportional-integral feedback with positive virtual impedance shaping to increase the frequency range of the equivalent virtual resistance up to the Nyquist

frequency. In this way, a grid-tied inverter will be highly stable regardless of changes in grid impedance.

The main contributions of the present paper include:

- Description of basic concepts and precise-designed of active damping control parameters based on capacitor-current proportional-integral positive feedback
- Simulation and extensive analysis of a grid-connected PV power conditioning system to ensure the performance and robustness of the proposed control system against grid and PV parameters variation.

The current paper addresses the following: The general description of the system, mathematical modeling, and AD based on CCF are examined in section two. Section three presents the performance of AD based on proportional-integral CCF. Section four focuses on the design of capacitor current feedback parameters and values for current regulators. Section five examines the power injection of the grid-connected solar system and the generation of reference current. In section six, the sample system is designed, and simulation results are presented. Finally, the paper concludes in section seven.

2. General Description of the System and Active Damping Based on Capacitor-Current Feedback

2.1. Description of the system and mathematical modeling

Figure 1 presents the structure of a PV system connected to a single-phase network using an LCL filter. In this figure, L_1, C, and L_2 form the LCL filter, and V_g represents the grid's voltage. An inductor and a resistor typically make up the network impedance at the point of common coupling (PCC). Because network resistance improves damping and contributes to system stability, a pure inductor L_g is considered to indicate the worst grid condition.

Based on the outline of the system under consideration, as shown in Figure 1, the block diagram of the grid-connected inverter control using the LCL filter by applying damping resonance based on CCF is demonstrated in Figure 2. Grid-connected inverters are designed to regulate the injected current to the grid (i_{L2}) sinusoidally and to regulate its phase using a point of common coupling voltage. Therefore, a phase-locked loop (PLL) is used to derive the phase angle of the V_{PCC}. Additionally, the reference current amplitude is calculated by setting the DC link voltage as I*. Gi(s) presents the current regulator. To determine the damping resonance of the LCL filter, the i_C capacitor-current is measured. H_{i1} and H_{i2} are the i_C and i_{L2} gains, respectively. The inverter transfer function is modeled by $K_{PWM} = V_{inv} / V_{tri}$. Here, V_{tri} represents the peak of the triangular carrier amplitude and V_{inv} represents the peak of the AC voltage generated by the inverter.

$G_d(s)$ indicates computational and PWM delays, which can be expressed as follows [12]:

$$G_d(s) \approx e^{-1.5sT_s} \quad (1)$$

In this case, T_s represents the sampling period. The proportional resonant controller (PR) is used by Equation 2 to minimize the steady-state error [12]:

$$G_i(s) = K_p + \frac{2K_r\omega_i s}{s^2 + 2\omega_i s + \omega_o^2} \quad (2)$$

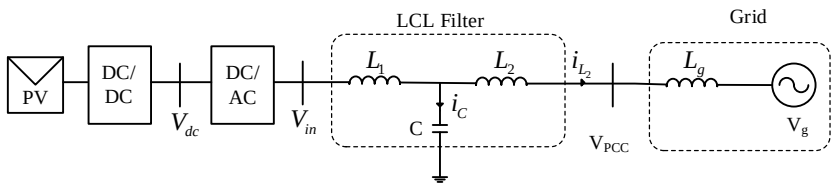

Figure 1. System outline

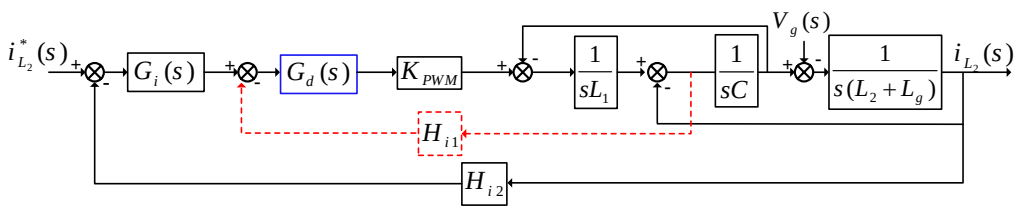

Figure 2. Digital control diagram of the grid-connected inverter with LCL filter and proportional capacitor-current AD

K_p indicates the proportional gain, K_r is the resonant gain, and $\omega_0 = 2\pi f_0$ is the principal component of the grid angular frequency, where ω_i indicates the bandwidth of the resonance section that reduces the sensitivity to changes in the base frequency.

In Figure 2, the gain of the T(s) loop is determined according to Equation 3.

$$T(s) = \frac{H_{i2}G_i(s)}{sL_1(L_2+L_g)C} \cdot \frac{K_{pwm}G_d(s)}{s^2 + s \cdot H_{i1}K_{pwm}G_d(s)/L_1 + \omega_r^2} \quad (3)$$

ω_r is the LCL angular resonance frequency, which is expressed as Equation 4.

$$\omega_r = 2\pi f_r = \sqrt{\frac{L_1+L_2+L_g}{L_1(L_2+L_g)C}} \quad (4)$$

2.2. Description of the system and mathematical modeling

The stability of the grid-connected inverter is usually evaluated by the Nyquist stability criterion according to the Z = P-2(N(+)-N(-)) equation. P and Z represented the number of right half-plane (RHP) poles of the open loop and closed loop transfer functions, respectively. Further, N(-) and N(+) indicate the number of negative and positive passes of -180 degrees, respectively. The necessary and sufficient condition for stability is Z=0.

When $H_{i1} = 0$, AD is not considered, as shown in Figure 3, and T(s) does not contain any open-loop poles in the right half-plane (RHP), i.e., P = 0. Nyquist stability requires N(+) - N(-) = 0 for the system to be stable. Under various values of L_g, Figure 3 displays T(s) without AD. According to this figure, there is a uniform decrease in the phase-frequency curve, so N(+) = 0. If $f_{res} \leq f_{sam}/6$, the negative passage happens in f_{res}, so N(-) =1, meaning stability has not been achieved. If $f_{sam}/6 < f_{res} < f_{sam}/2$, the curve of phase-frequency for T(s) passes through -180 degrees at $f_{sam}/6$ due to the phase delay caused by $G_d(s)$. As a result of the phase delay generated by $G_d(s)$, the curve of phase-frequency for T(s) passes through -180 degrees at $f_{sam}/6$ if $f_{sam}/6 < f_{res} < f_{sam}/2$. Additionally, this will not be a negative pass when the T(s) gain at $f_{sam}/6$ is lower than zero dB. By adjusting the proportional gain K_p, this can be accomplished.

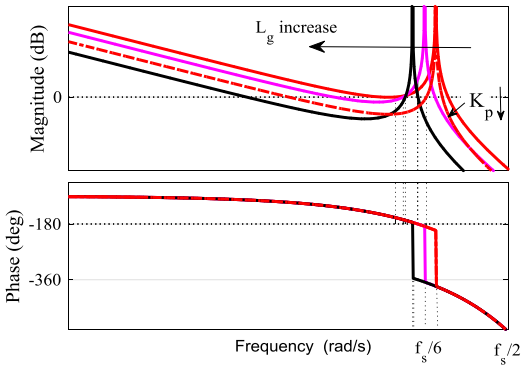

Figure 3. Bode diagram of single-loop current control loop gain

Substituting $s = j2\pi f_{sam}/6$ at Equation 3 and assuming $|T(j2\pi f_{sam}/6)| < 0$ dB, Equation 5 is obtained.

$$K_p < \frac{L_1(L_2+L_g)C}{H_{i2}K_{pwm}} \cdot 2\pi \frac{f_s}{6}\left[(2\pi f_r)^2 - (2\pi \frac{f_s}{6})^2\right] \quad (5)$$

This means that reducing the proportional gain will ensure system stability, but may compromise dynamic performance [34].

According to the analysis, maintaining the LCL resonant frequency within the $[f_{sam}/6, f_{sam}/2]$ range is a simple method to ensure inverter stability against changes in grid impedance. This can be achieved by replacing the inverter side inductor and the filter capacitor resonant frequency as $f_{r\infty}$, higher than $f_{sam}/6$. Actually, $f_{r\infty}$ is the LCL resonant frequency when L_g is a large value. Simplicity makes this method interesting, but it is critical to design the LCL filter properly. Accordingly, for low-voltage consumer applications, iron powder cores are commonly used in filter inductors. Due to the soft permeability, the value of the filter inductors varies in a wide range. Considering that the minimum value of inductor L_1 determines the permissible current ripple for the inductor, in this case, the condition $f_{r\infty} > f_{sam}/6$ needs to be met under the maximum value of inductor L1, making it necessary to use a reasonably small capacitor C. Due to the harmonic reduction of the switching frequency, L_2 may be a relatively large and bulky filter. Comparatively, when damping is applied, the $f_{r\infty} > f_{sam}/6$ condition is not necessary, so choosing the filter parameters is much easier and will help minimize the filter size. Here, a suitable damping method is investigated.

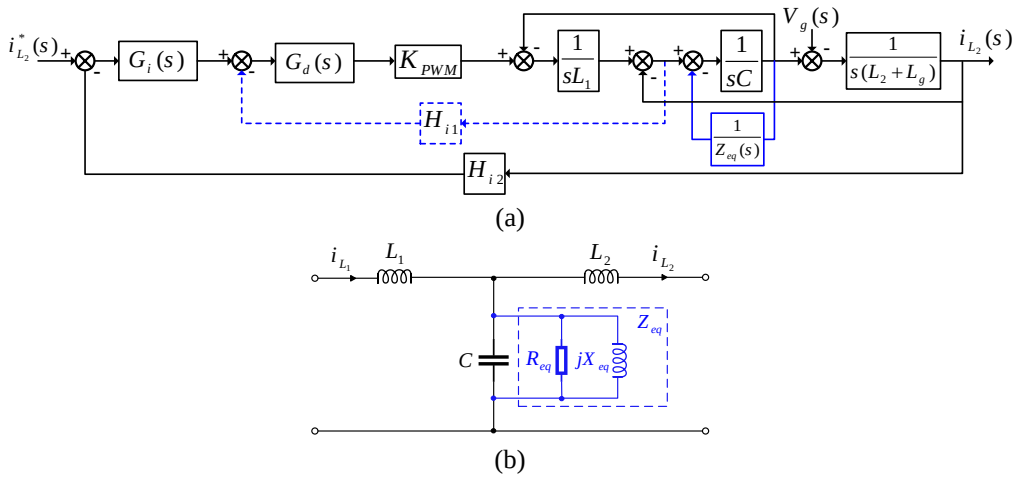

Figure 4. Inverter diagram with proportional AD capacitor-current, (a) block diagram, (b) equivalent circuit.

2.3. Active damping based on capacitor-current feedback

Active damping of proportional CCF has attracted much attention due to its simplicity. Using the variations depicted in Figure 4(a), which is derived from Fig 2, the proportional CCF AD, according to Figure 3(b), is equivalent to a virtual Z_{eq} impedance parallel to the filter capacitor C. The virtual impedance equivalent to Z_{eq} is expressed according to Equation 6.

$$Z_{eq}(s) = \frac{L_1}{H_{i1}K_{pwm}C}.\frac{1}{G_d(s)} \tag{6}$$

Substituting s = jω in Equation 6 gives the Equation 7:

$$Z_{eq}(\omega) = \frac{L_1}{H_{i1}K_{pwm}C}.e^{1.5\,j\omega T_s} \square\, R_{eq}(\omega) \,||\, jX_{eq}(\omega) \tag{7}$$

In which:

$$R_{eq}(\omega) = \frac{L_1}{H_{i1}K_{pwm}C\cos(1.5\omega T_s)} \tag{8}$$

$$X_{eq}(\omega) = \frac{L_1}{H_{i1}K_{pwm}C\sin(1.5\omega T_s)} \tag{9}$$

According to Equation 7 and Figure 4(b), Z_{eq} is a parallel connection of the R_{eq} resistor and X_{eq} reactance. Both the R_{eq} and X_{eq} parameters are frequency-dependent. R_{eq} helps attenuation damping, and X_{eq} makes the system resonant frequency (f_{res}) different from the filter resonant frequency (f_r').

The frequency characteristics of R_{eq} and X_{eq}, when H_{i1} is positive, are displayed in Figure 5, according to Equations 8 and 9. As shown in the figure, R_{eq} has a positive value in the [0, f_{sam}/6] and a negative value in the [f_{sam}/2, f_{sam}/6] frequency range. Additionally, X_{eq} has a capacitive behavior in the [f_{sam}/2, f_{sam}/3] frequency range. Conversely, in cases where H_{i1} is negative, R_{eq} has a negative value in the [0, f_{sam}/6] and a positive value in the [f_{sam}/2, f_{sam}/6] frequency range. Besides, X_{eq} has capacitive behavior in the [0, f_{sam}/3] and inductive behavior in the [f_{sam}/2, f_{sam}/3] frequency range.

Based on the previously mentioned analysis and the results in [28], it can be concluded that it is not essential, whether H_{i1} is positive or negative; what matters is that the equivalent resistance value is positive in the [0, f_{sam}/2]. If the $R_{eq}(f_r')$ is negative in the [0, f_{sam}/2] frequency range, the system will be unstable. Therefore, it is necessary to use a suitable damping method to ensure that R_{eq} is positive in the whole [0, f_{sam}/2] desired frequency range. Under these conditions, the stability of the inverter against network impedance changes increases significantly.

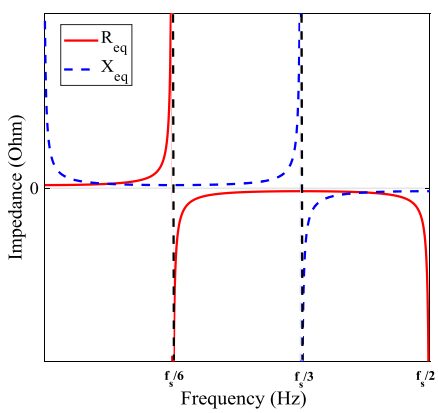

Figure 5. Frequency characteristic of R_{eq} and X_{eq} when H_{i1}> 0.

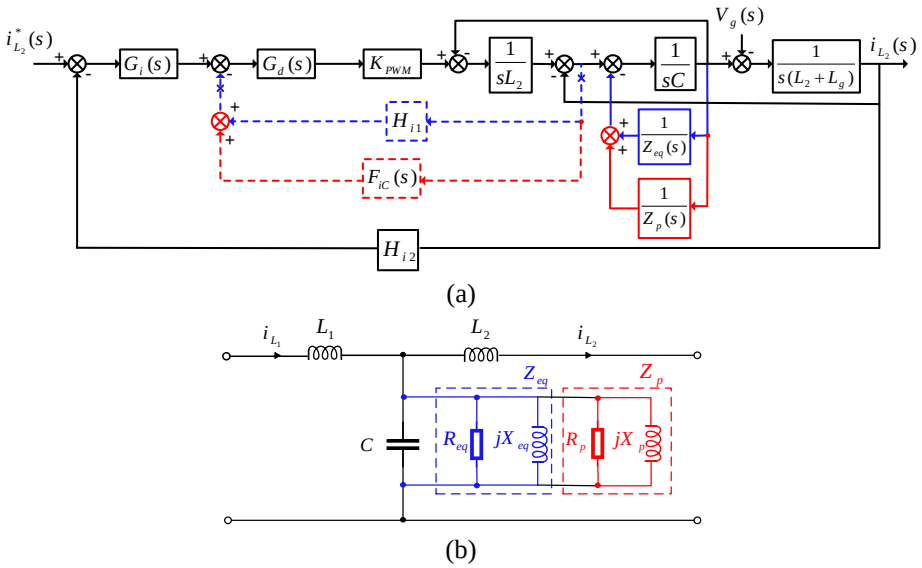

Figure 6. Scheme of the grid-tied inverter with added parallel impedance, (a) diagram of the control system, (b) equivalent circuit

3. Active Damping Based on the Proportional-Integral Capacitor-Current Positive Feedback

3.1. Basic concepts

To achieve a positive equivalent resistance across the controllable frequency range, a simple idea, as shown in Figure 6(a), is to add a feedback function in parallel with H_{i1}. Through block equivalent conversion, this additional feedback is equivalent to a Z_p impedance connected via a parallel connection to the primary Z_{eq} equivalent impedance. Figure 6(b) demonstrates the equivalent circuit of the grid-connected inverter considering the additional virtual impedance Z_p.

Z_p can be presented as a parallel connection between the R_p resistor and the X_p reactance. Accordingly, the R'_{eq} and X'_{eq} are the equivalent resistance and the equivalent reactance, respectively, which are expressed according to Equations 10 and 11.

$$R_{eq}'(\omega) = R_{eq}(\omega) \,||\, R_p(\omega) = \frac{R_{eq}(\omega)R_p(\omega)}{R_{eq}(\omega)+R_p(\omega)} \tag{10}$$

$$X_{eq}'(\omega) = X_{eq}(\omega) \,||\, X_p(\omega) = \frac{X_{eq}(\omega)X_p(\omega)}{X_{eq}(\omega)+X_p(\omega)} \tag{11}$$

It is clear that R_p and X_p depend on frequency. Based on Equation 10, a favorable R_p can help ensure a positive R'_{eq} over the entire range of controllable frequencies. To achieve this, an appropriate feedback function of the capacitor-current must be chosen.

3.2. Proper performance of capacitor-current feedback

According to Figure 6(a), the CCF function consists of H_{i1} and F_{iC}. This means that a good F_{iC} is required to comply with H_{i1}. There are several types of F_{iC} to choose from. Nevertheless, the simple and common integral expression is $F_{iC}(s) = K/s$, K is the integral coefficient in this case. As a result, a proportional-integral controller (PI) is used to feed the capacitor current. Here, the H_{i1} and K symbols must be similar. Otherwise, the feedback function has a complex right half-plane zero (RHP), which results in a non-minimum phase characteristic. As a result, the examination of the two cases should be considered according to Table 1.

Fig 6(a) illustrates the equivalent block diagram that enables easy extraction of the R_P expressions associated with the integral term, presented in Table 1. Figure 7 illustrates the R_{eq} and R_p frequency characteristics for the proportional-integral controller in two K> 0, H_{i1}> 0 and K<0, H_{i1} <0 modes. As shown in Figure 7(a), in the [f_{sam}/3, f_{sam}/6] frequency range, resistors R_{eq} and R_p are both negative. Therefore, R'_{eq} should be negative according to Equation 10. This means that condition (a) does not create favorable conditions. As displayed in Figure 7(b), in the [f_{sam}/3, f_{sam}/6] frequency range, the resistors R_p and R_{eq} are both positive, so R'_{eq} is positive definite. In Figure 7(b),

R_{eq} and R_p have opposite signs in other frequency ranges. Based on Equation 10, R'_{eq} is positive if $R_{eq}+R_p<0$. By replacing the R_p and R_{eq} specified in Table 1 in the $R_{eq}+R_p=0$, the positive boundary frequency for R'_{eq}, which is shown as f_{Rb}, can determine that $H_{i1}/K=1.5T_s$, f_{Rb} is approximately equal to $0.48f_{sam}$. This means that the upper limit of the frequency range for the positive R'_{eq} is increased to approximately $f_{sam}/2$. Consequently, the AD of the positive CCF exhibits good performance using the proportional-integral controller H_{i1} + K/s (K <0, H_{i1} <0).

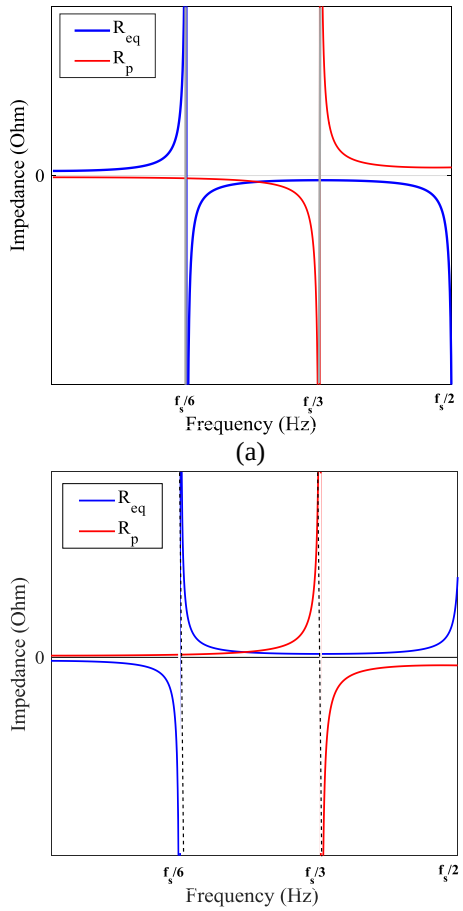

Figure 7. Frequency response characteristic of R_{eq} and R_p in the presence of proportional-integral controller in the positive CCF path, (a) H_{i1}> 0, K> 0, (b) H_{i1} <0, K <0

3.3. Active damping based on positive proportional-integral capacitor-current feedback

In this section, the equivalent impedance of the positive proportional-integral capacitor-current implementation of feedback AD is examined.

Table 1. The range of positive equivalent resistance at its highest frequency with PI feedback

Feedback condition	H_{i1}+ K/s	
	K>0 , H_{i1}>0	K<0 , H_{i1}<0
R_{eq}	$\frac{L_1}{H_{i1}K_{pwm}C\cos(1.5\omega T_s)}$	
R_p	$-\frac{L_1\omega}{K\cdot K_{pwm}C\sin(1.5\omega T_s)}$	
Maximum frequency range of positive R'_{eq}	$(0,f_{sam}/6)$ or $(f_{sam}/3,f_{sam}/2)$	$(0,f_{sam}/2)$

R'_{eq} and X'_{eq} frequency characteristics for the AD of the positive proportional-integral CCF are plotted in Figure 8. According to this figure, R'_{eq} has a positive value in the [0, f_{Rb}] and a negative value in the [f_{Rb}, $f_{sam}/2$] frequency range. X'_{eq} has capacitive properties in the [0, f_{Xb}] and inductive properties in the [f_{Xb}, $f_{sam}/2$] frequency range, which f_{Xb} represents the boundary frequency of X'_{eq}. As mentioned, the maximum frequency of the positive equivalent resistance, f_{Rb}, has increased nearly $f_{sam}/2$. Thus, a minimum phase response of the system is guaranteed, which leads to an increase in the stability of the grid-connected inverter against the network impedance changes.

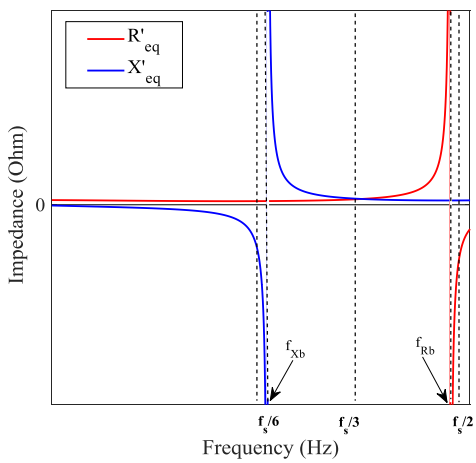

Figure 8. Frequency characteristic of R'_{eq} and X'_{eq} for the positive proportional-integral CCF active damping

4. Design of Control Parameters

According to the topics discussed in Section 3, the controlling parameters of the CCF function and the current regulator must be adjusted correctly to

ensure $R_{eq}(f_r')> 0$. This section presents the control parameters design.

4.1. Decoupled two-loop model

The loop gain T(s) demonstrated in Equation 3 is rewriteable as follows:

$$T(s)=\frac{H_{i2}G_i(s)}{s^2(L_2+L_g)C}\cdot\frac{G_{iC}(s)}{1+H_{i1}(s)G_{iC}(s)} \quad (12)$$

In which:

$$G_{iC}(s)=\frac{K_{pwm}G_d(s)s}{L_1(s^2+\omega_r^2)} \quad (13)$$

Since the $G_i(s)$ current regulator does not have the imaginary axis right-half plane pole RHP, the number of RHP poles of loop gain is expressed by the following Equation:

$$\varphi_{iC}(s)=\frac{G_{iC}(s)}{1+H_{i1}(s)G_{iC}(s)} \quad (14)$$

As can be seen in Equation 14, φ_{iC} is similar to a closed-loop system in that the feedforward and feedback transfer functions are $G_{iC}(s)$ and $H_{i1}(s)$, respectively. By considering Equations 12 and 14, it is possible to construct an equivalent control diagram according to Figure (9). If the internal loop is stably designed, the external loop will not include the open-loop right pole. Therefore, in the Nyquist stability discussion, the number of right half-plane poles of the open-loop conversion function will be zero (P = 0). Hence, the internal loop parameters or the CCF parameters can be designed separately to warranty P=0. Afterward, the external loop parameters or the same parameters of the current regulator could be adjusted to guarantee system stability.

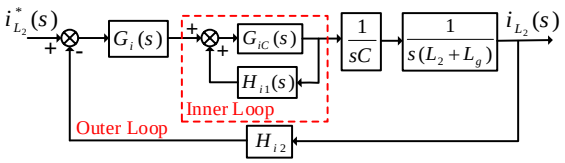

Figure 9. Equivalent control block diagram of the grid-connected inverter with LCL filter with positive proportional-integral CCF AD

4.2. Capacitor-current feedback parameters design

Based on Figure 9, the $T_{iC}(s)$ internal loop gain is obtained as follows:

$$T_{iC}(s)=H_{i1}(s)G_{iC}(s)=\frac{K_{pwm}(H_{i1}s+K)}{L_1(s^2+\omega_r^2)}e^{-1.5sT_s} \quad (15)$$

Thus, the stability of the internal loop could be evaluated using Nyquist stability criteria, i.e., P_i-2(N_i(+) - N_i(-)) = 0, where N_i(+) and N_i(-) present the number of positive and negative internal loop intersections, and P_i represents the number of right half-plane poles (RHP) of the open-loop conversion function of the internal loop. As shown in (15), $T_{iC}(s)$ does not contain the RHP pole, and P_i = 0 is established. Therefore, N_i(+) - N_i(-) = 0 must be satisfied so that the internal loop is independently stable.

Figure 10 depicts the Bode diagrams of the internal loop gain. In the low-frequency range, the magnitude curve of $T_{iC}(s)$ has a zero slope, and the phase curve gradually decreases from 180° in the low-frequency range. In addition, when the filter resonant frequency (f_{res}) is reached, the magnitude curve shows an infinite resonance peak. The phase curve decreases in the corresponding frequency range and passes through the -180° at the f_{Rb} frequency. As a result, two gain margins, including GM_{i1} and GM_{i2}, must be observed to avoid negative zero-crossings at zero and f_{Rb} frequencies, respectively. Meanwhile, the PM_{i1} and PM_{i2} two-phase margins are defined at the crossover frequencies of phase f_{c_i1} and f_{c_i2}, respectively. It should be noted that with the realization of the PM_{i2} phase margin, the G_{Mi2} gain margin is realized naturally. Because the size of the open-loop conversion of the internal $T_{iC}(s)$ control loop decreases uniformly in the [f_{c_i2}, $f_{sam}/2$] frequency range.

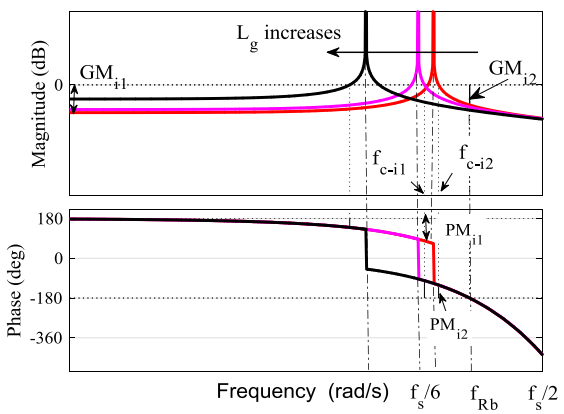

Figure 10. Internal loop bode diagram of the positive proportional-integral CCF AD

$$K_{GM1} = 10^{\frac{GM1}{20}} . \frac{L_1 (2\pi f_r)^2}{K_{pwm}} \tag{16}$$

$$K_{PMi1} = H_{i1} . 2\pi f_{c\_i1} . \tan(PM_{i1} - \frac{\pi}{2} - 3\pi f_{c\_i1} T_s) \tag{17}$$

$$K_{PMi2} = H_{i1} . 2\pi f_{c\_i2} . \tan(-PM_{i2} + \frac{\pi}{2} - 3\pi f_{c\_i2} T_s) \tag{18}$$

$$f_{c\_i1} = \frac{1}{2\pi} \sqrt{(2\pi f_r)^2 + \frac{K_{pwm}^2 H_{i1}^2 - \sqrt{K_{pwm}^4 H_{i1}^4 + 4L_1^2 K_{pwm}^2 H_{i1}^2 (2\pi f_r)^2 + 4L_1^2 K_{pwm}^2 K^2}}{2L_1^2}} \tag{19}$$

$$f_{c\_i2} = \frac{1}{2\pi} \sqrt{(2\pi f_r)^2 + \frac{K_{pwm}^2 H_{i1}^2 + \sqrt{K_{pwm}^4 H_{i1}^4 + 4L_1^2 K_{pwm}^2 H_{i1}^2 (2\pi f_r)^2 + 4L_1^2 K_{pwm}^2 K^2}}{2L_1^2}} \tag{20}$$

$$K_{PMi1,2} = -\sqrt{\left(4\pi^2 \lambda_{1,2}^2 f_r^2 H_{i1}^2 + \frac{(\lambda_{1,2}^4 + \lambda_{1,2}^2) K_{pwm}^2 H_{i1}^4}{2L_1^2}\right) + \sqrt{\left(4\pi^2 \lambda_{1,2}^2 f_r^2 H_{i1}^2 + \frac{(\lambda_{1,2}^4 + \lambda_{1,2}^2) K_{pwm}^2 H_{i1}^4}{2L_1^2}\right)^2 - (4\pi^2 f_r^2 L_1 H_{i1})^2}} \tag{21}$$

Based on $GM_{i1} = -20\lg | T_{iC}(j2\pi \cdot 0) |$, the boundary value of the coefficient K, which is limited by the gain margin of the internal loop, is obtained from Equation 16. Given that $PM_{i1} = \pi - \angle T_{iC}(j2\pi f_{c\_i1})$ and $PM_{i2} = \angle T_{iC}(j2\pi f_{c\_i2}) - (-\pi)$, the boundary value of the coefficient K in terms of H_{i1}, which is limited by the phase margins of the internal loop, is obtained from Equations 17 and 18. Therefore, $f_{c\_i1,2}$ can be derived from $T_{ic}(j2\pi f_{c\_i1,2})|=1$. Corresponding relationships with the $f_{c\_i1,2}$ phase intersection frequencies can be expressed according to Equations 19 and 20. Considering that the approximation $\tan(3\pi f_{c\_i1,2}T_s) \approx \tan(3\pi f_{res} T_s)$ is valid due to the proximity of the gain crossover frequencies $f_{c\_i1,2}$ to the filter resonant frequency f_r, by replacing Equations 19 and 20 in Equations 17 and 18, respectively, Equation 21 is obtained, in which:

$$\lambda_1 = \tan(\frac{\pi}{2} + 3\pi f_r T_s - PM_{i1}) \tag{21.a}$$

$$\lambda_2 = \tan(-\frac{\pi}{2} + 3\pi f_r T_s + PM_{i2}) \tag{21.b}$$

If GM_{i1}, PM_{i1}, and PM_{i2} are specified, an acceptable range of K in terms of H_{i1} is determined from Equations 16 and 21. In addition, it should be noted that the optimum phase and gain margin for the internal loop must be satisfied throughout the L_g network impedance range. As shown in Figure 10, with increasing L_g, the GM_{i1} and PM_{i1} decrease, and PM_{i2} increases. This means that the satisfactory range boundaries for the K coefficient should be obtained by GM_{i1} and PM_{i1} at the maximum value of L_g and by PM_{i2} at the minimum value of L_g. The gain and the phase margin should not be less than 3 dB and 30°, respectively [15].

4.3. Current regulator parameters design

There are three parameters ω_i, K_p, and K_r, that must be designed based on Equation 2. To deal with ±1% changes in the base frequency of the network [8], $\omega_i = \%1 \times 2\pi f_o = \pi$ rad/s is set. K_r and K_p are generally set assuming $L_g = 0$ [28]. By assuming $|T(j2\pi f_c)| = 1$, the value of K_p bounded by f_c is calculated [15], which can be expressed by Equation 22:

$$K_p \approx \frac{2\pi f_c (L_1 + L_2)}{H_{i2} K_{pwm}} \tag{22}$$

To lessen the phase delay of the PR controller at the gain crossover frequency, the $G_i(s)$ corner frequency should be set to 10% of the gain crossover frequency f_c [35]. As a result, the optimal K_r is equal to the following relation:

$$K_r = \frac{2\pi f_c}{10} . \frac{K_p}{2\omega_i} \tag{23}$$

Based on Equations 22 and 23, the appropriate K_p and K_r are determined based on the value of f_c. The highest possible value of f_c is constrained by the desired PM so that, considering $f_c \approx 4 f_{sam}$ with a phase limit (PM) of about 60 degrees, creates a favorable condition, and a small percentage of overshoot is expected under these conditions [36]. In the next step, it is essential to examine the external loop gain margin (GM). If the required conditions are not satisfied at the external loop gain margin, f_c must be readjusted, which will correct the K_p and K_r values.

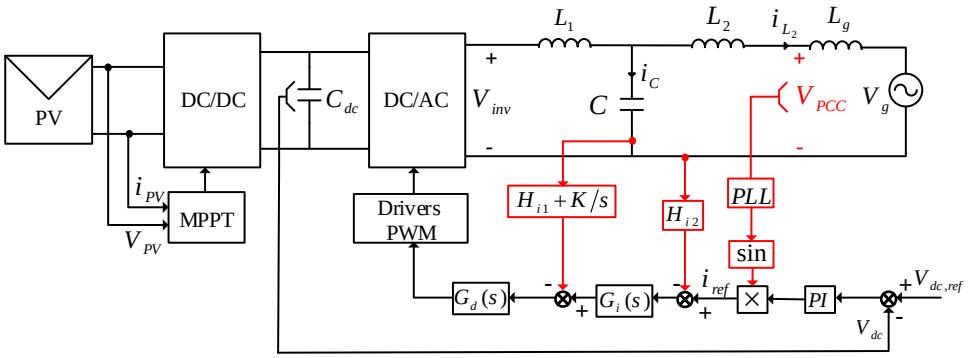

Figure 11. Grid-connected solar system control structure

5. Power Injection Control of the Grid-Connected Solar System

The controller structure and the power injection mechanism for the grid-connected solar system are shown in Figure 11. As shown, a boost converter is used to increase the solar array voltage and track the maximum power of its. In this section, the maximum power point tracking algorithm and reference current generation using the boost converter output DC link are presented.

5.1. Maximum power point tracking

Maximum power point tracking using the incremental conductance (IC) method depends on the fact that the first derivative of the P-V curve is zero at the maximum power point, which means dP/dV = 0. In solar arrays, the current in a photovoltaic cell depends on the voltage level. Thus, the derivative of P = I (V)* V is dP/dV=V×(dI/dV)+I(V). By setting this equation to zero, dI/dV = I(V)/V is obtained. The maximum power point is obtained when the incremental conductance equals the negative instantaneous conductance. The voltage corresponding to the point dI/dV=-I(V)/V is known as the maximum power point voltage. The controller maintains this voltage until the sunlight changes and the method is repeated [37].

Since an integral unit eliminates the remaining steady-state error in the controller, an integrator is utilized to reduce the error signal. The (e) error signal is the sum of instantaneous conductance (I/V) with incremental conductance (dI / dV).

$$e = I/V + dI/dV \quad (24)$$

As shown in Figure 12, the integral regulator collects the instantaneous error, then multiplies it by the integral gain and adds it to the controller output [38].

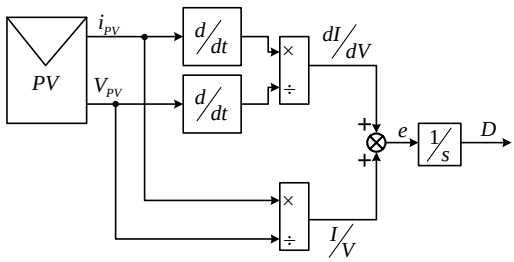

Figure 12. Maximum power point tracking error signal generating method

5.2. Control of injected reference current into the grid

Figure 13 shows how to generate and control the injected reference current into the grid. Since the injected current to the grid must follow the reference current, the voltage error signal resulting from the difference between the voltage generated by the boost converter and the DC link reference voltage value is given to a PI regulator. Proper adjustment of PI controller parameters will result in good performance of the controller. The output of the PI controller, as shown in Figure 13, is the size of the reference current injected into the grid. It is worth noting that the reference current phase is measured by the PLL unit installed at the common connection point (PCC).

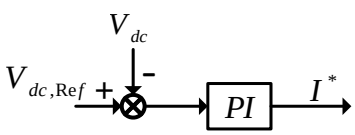

Figure 13. Controlling schematic of the injected reference current into the grid

6. Sample Design and Simulation Results

6.1. A sample system design

Table 2 presents the parameters of a 2.4 kW single-phase LCL grid-connected inverter. For the evaluation of the proposed damping method, a high resonant frequency LCL filter f_{r0} = 6.27 kHz was utilized. The robustness of the system has been investigated by changing the L_g to 10% per unit, which is equivalent to 2.6 mH. Given the above values for the internal loop gain and phase margin, the acceptable area for K and H_{i1} can be plotted as depicted in Figure 14. A set of suitable parameters, H_{i1} = -0.05, and K = −1500 are selected corresponding to point A. By replacing $f_c \approx \%4 f_{sam}$ = 800 Hz into Equations 22 and 23, K_p = 0.7158 and K_r = 57.2610 are computed.

Table 2. The values of the under-consideration system parameters

Parameter	Symbol	Value
Grid voltage	V_g	220V
Output power	P_o	4.2KW
Base frequency	f_o	50Hz
Switching frequency	f_{sw}	10KHz
Resonance frequency	f_{res}	6.27KHz
Sampling frequency	$f_s=f_{sam}$	20KHz
Inverter side inductor	L_1	826µH
Grid side inductor	L_2	200µH
Filter capacitor	C	4µf
DC link capacitor	C_{DC}	6700µf
Triangular carrier signal amplitude	V_{tri}	4.58V
Grid current sensor gain	H_{i2}	0.15

Based on the defined parameters, the internal and external loop diagrams can be illustrated according to Figure 15. According to this figure, the minimum gain of the internal loop and the phase margin under two normal network impedance situations are 6.4 dB and 31°, respectively. In contrast, the minimum gain of the external loop of the gain margin and phase margin is 8.66 dB and 64°, respectively. Thus, both loops have good stability margins, and this confirms the effectiveness of the design method.

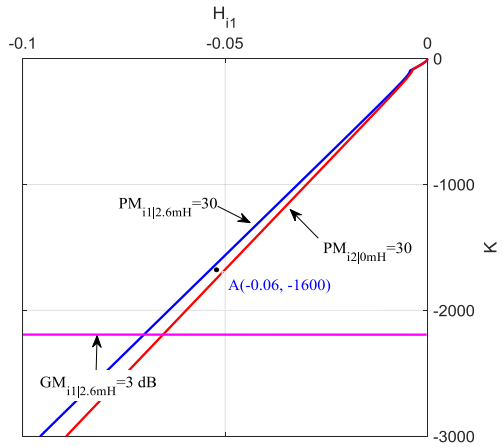

Figure 14. Satisfactory and stable region for H_{i1} in terms of K

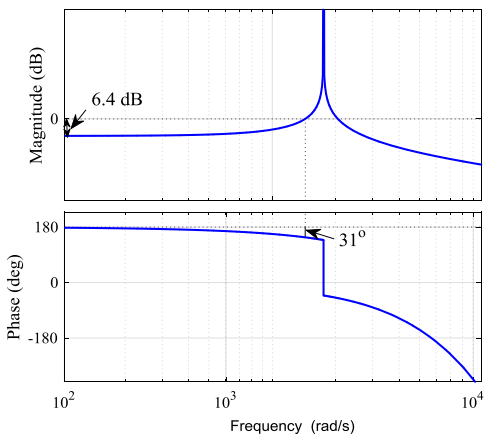

(a)

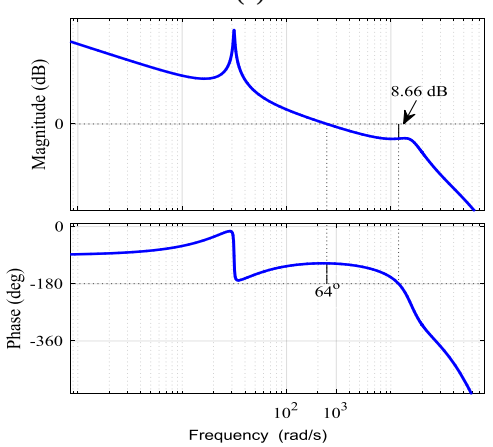

(b)

Figure 15. Bode diagram of a two-loop system, (a) internal loop gain, (b) external loop gain

Figure 16 demonstrates the distribution of open loop and closed loop poles based on the change in L_g grid impedance. In this analysis, the closed-loop pole pair resulting from the PR regulator is not shown due to their small changes. As displayed in Figure 16(a), both pairs of inverter's open loop poles with the proportional-integral CCF damping method are always inside the unit circle and lead to P≡0. Figure 16(b) shows that the closed-loop poles of the inverter with the proportional-integral CCF damping are inside the unit circle, away from its boundaries. This indicates that a sufficient stability margin is obtained using this damping method even for f_{res} close to or equal to $f_{sam}/6$. Therefore, the proportional-integral CCF damping method increases the inverter stability against the changes in network impedance and improves dynamic performance.

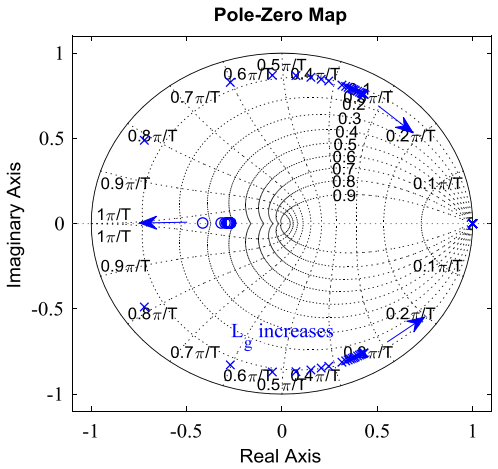

(a)

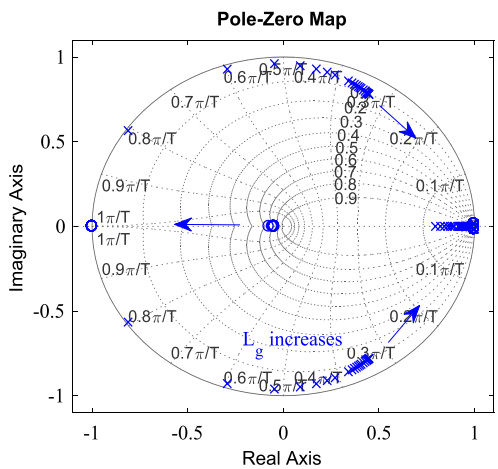

(b)

Figure 16. Grid-connected pole-zero map with changes in network impedance, (a) open loop pole-zero map, (b) closed loop pole-zero map

6.2. Stability and sensitivity analysis for changes in LCL filter parameters

Investigating the stability of a power system is one of the most critical studies in a power grid. Several studies have evaluated the sensitivity and stability of power systems. LCL filter parameters, which include inductors and capacitors, deteriorate and lose their inductance and capacitance over time. The change in the value of the LCL filter parameters is defined as $C+\Delta C$, $L_1+\Delta L_1$, and $L_2+\Delta L_2$.

Sensitivity analysis is performed to investigate the function of the power conditioning system for changing the values of LCL filter parameters by 5%, 10%, and 15% and their effect on the stability of internal and external loops of the system as well as the THD of the grid current.

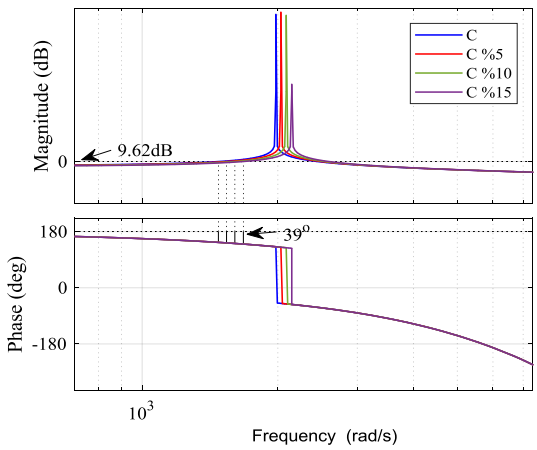

(a)

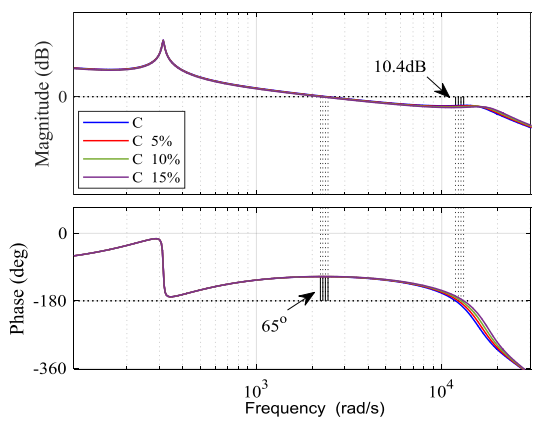

(b)

Figure 17. Bode diagram of a two-loop system with changes in the LCL filter capacitor value, (a) internal loop gain, (b) external loop gain

Figure 17 illustrates a bode diagram of an internal and external loop for the changes of the

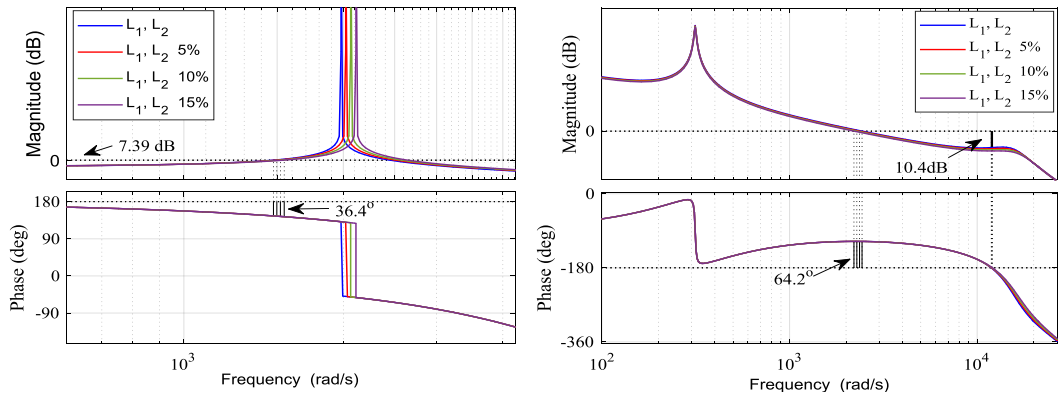

(a) (b)

Figure 18. Bode diagram of a two-loop system with changes in the LCL filter inductors values, (a) internal loop gain, (b) external loop gain

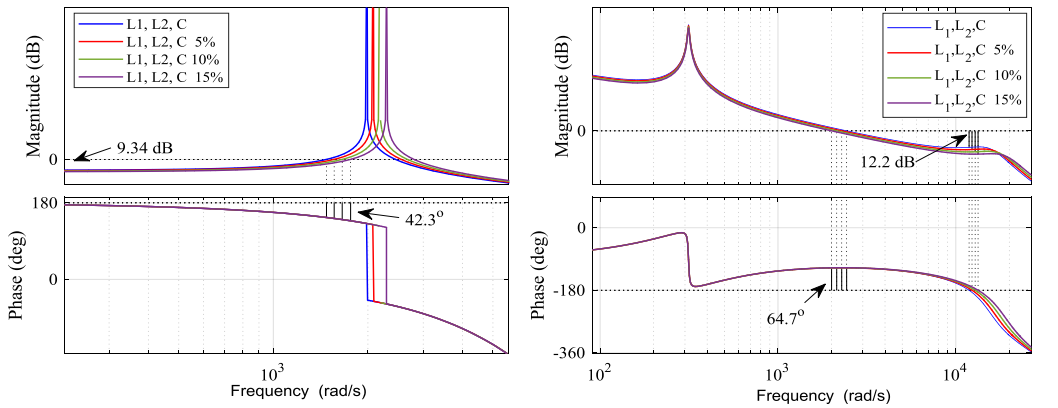

(a) (b)

Figure 19. Bode diagram of a two-loop system with changes in the LCL filter capacitor and inductors values, (a) internal loop gain, (b) external loop gain

Table 3. Injected current THD for changes in LCL filter parameter values

Parameter	Parameters variations	THD%
L_1, L_2	5٪	1.91
	10٪	2.10
	15٪	2.14
C	5٪	1.76
	10٪	1.78
	15٪	1.78
L_1, L_2, C	5٪	1.92
	10٪	2.12
	15٪	2.12

LCL filter capacitor. It is clear that by reducing the value of the capacitor from 5% to 15%, the system still maintains its stability and is not sensitive to changes in the value of the capacitor.

Changes in the LCL filter inductors values with a reduction of 5% to 15% and their effect on the stability of internal and external loops are demonstrated in Figure 18. Fig 18 shows that by changing the inductor value, the system maintains stability.

Figure 19 shows the state in which all three LCL filter parameters, L_1, L_2, and C, change simultaneously. Figure 19 reveals that with decreasing inductors and capacitor values, the gain and phase margin requirements remain the same, and the system is stable.

The THD analysis of the grid current concerning changes in the LCL filter capacitor and inductors values is shown in Table 3. Changes of 5%, 10%,

and 15% in the parameter values cause the THD of the injected current to increase slightly. According to Table 3, when only the value of the filter capacitor changes, the grid current THD changes very small and can be ignored. However, it increases with the change in the values of the inductors. Due to the simultaneous reduction of the LCL filter parameter values by 5%, 10%, and 15%, the THD of the grid current increases by 9%, 20.45%, and 20.45%, respectively.

6.3. Simulation results

Power generation systems using solar panels are often used in low-voltage networks. As previously discussed, in low-voltage networks, the network impedance is constantly changing. In addition, changes in weather conditions must be considered in the design. In order to model these conditions and indicate the correct operation of the control system, the worst-case impedance of the network, i.e., pure inductive, is considered at 2.6 mH. Additionally, changes in weather conditions with decreasing radiation intensity from 1000 W/m^2 to 800 W/m^2 have been considered in this study. The values for the utilized parameters in the solar panel design are shown in Table 4.

Table 4. Solar panel parameters at 25°C and 1000W/m^2 radiation intensity.

Parameter	Value
I_{mp}	4.5 A
V_{mp}	54.2 V
P_{max}	259.39 W
I_{sc}	5.83 A
V_{oc}	63.3 V
N_s	3
N_p	5

Figure 20(a) shows the P-V curve for the solar array for two different radiation intensities, 1000 W/m^{2,} and 800 W/m^2. The reduction in radiation intensity is shown in Figure 20(b). According to this figure, the radiation intensity has decreased from 1000 W/m^2 to 800 W/m^2 within [0.5, 0.7] time interval. Throughout [0.7, 1.1] seconds, the radiation intensity remained constant at 800 W/m2, and over the next [1.1, 1.3], it increased from 800 W/m2 to 1000 W/m2.

Figure 21 illustrates the power generated by the solar panel. Figure 21 shows that as radiation intensity decreases from 1000 W/m2 to 800 W/m2, PV power decreases from 4200 W to 3400 W over the [0.5, 1.3] time interval.

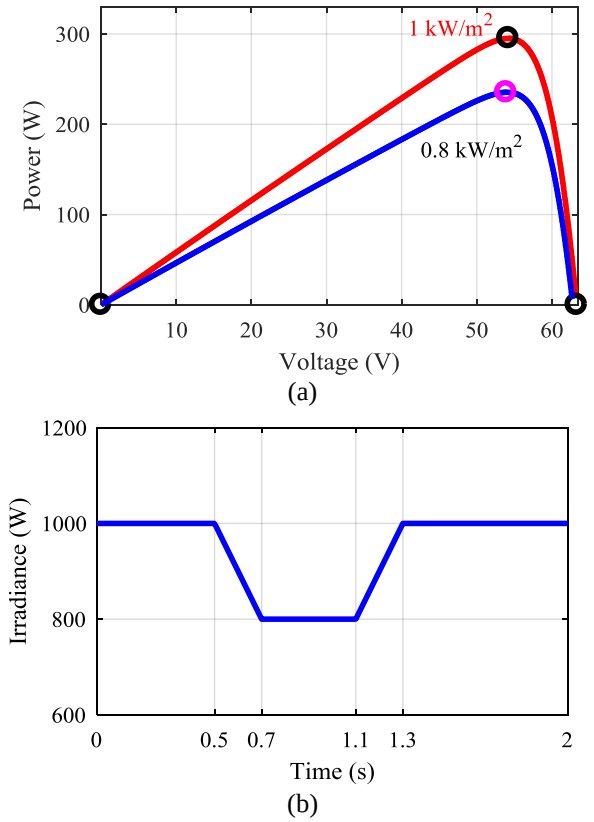

Figure 20. (a) P-V curve of the solar panel, (b) changes in radiation intensity.

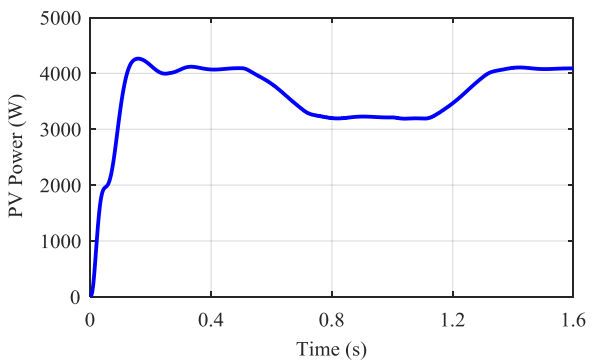

Figure 21. PV production power.

The voltage generated by the solar panel is shown in Figure 22(a). The voltage ripple is considerably low, indicating the successful tracking of the maximum power point with changes in weather conditions. The DC link voltage of the boost converter output is shown in Figure 22(b). As shown, the DC link voltage of the boost converter output has tracked closely with the reference voltage ($V_{dc.\ Ref}$ = 360).

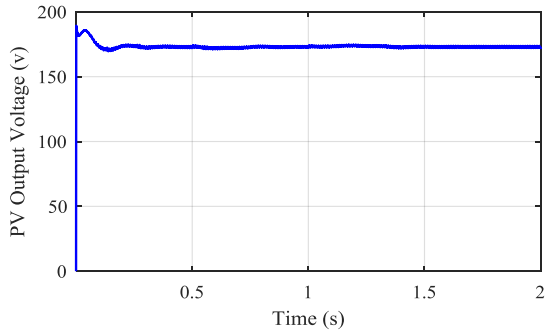

(a)

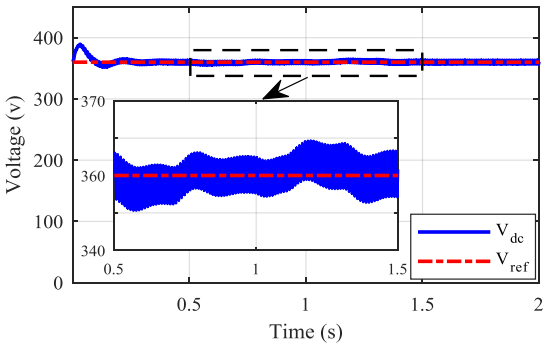

(b)

Figure 22. (a) Voltage waveform generated by the solar panel, (b) boost converter output voltage

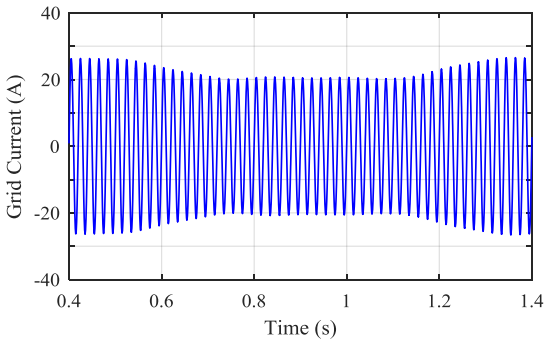

(a)

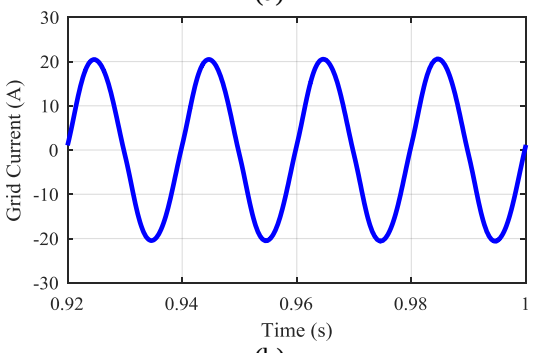

(b)

Figure 23. (a) Injected current waveform, (b) injected current waveform within [0.92, 1] time interval

Grid-connected inverter control systems are designed to inject sine current into the grid, as described in the previous section. Figure 23(a) displays the current injected into the network.

According to this figure, the injected current has a sinusoidal waveform. Besides, by reducing the radiation intensity within [0.5, 1.3] time interval, the current waveform retains its sinusoidal shape, which indicates the stability of the system against radiation intensity changes. Figure 23(b) shows the injected current in the mentioned time interval.

The network voltage and current waveforms at the common connection point are shown in Fig 24(a). According to this figure, current and voltage waveforms are sinusoidal, with no phase difference between them. The network current fast Fourier transform (FFT) is shown in Figure 24(b) with a THD of 1.76%.

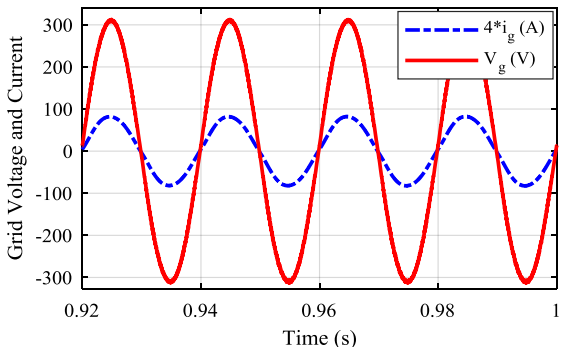

(a)

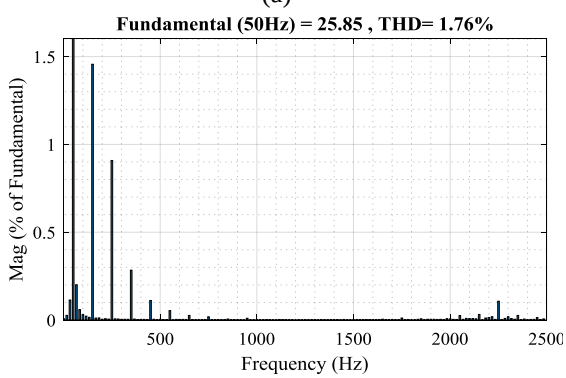

(b)

Figure 24. (a) Grid voltage and current waveform, (b) THD of the injected current into the grid

Figure 25 shows how much solar power is delivered to the grid by the solar power conditioning system. According to the PV power reduction, the output power of the network also decreases due to the reduction of radiation intensity within [0.5, 1.3] time interval. By reducing the radiation intensity

from 1000 W/m^2 to 800 W/m^2, the power delivered to the network decreases from 4000W to 3150W in the same time interval.

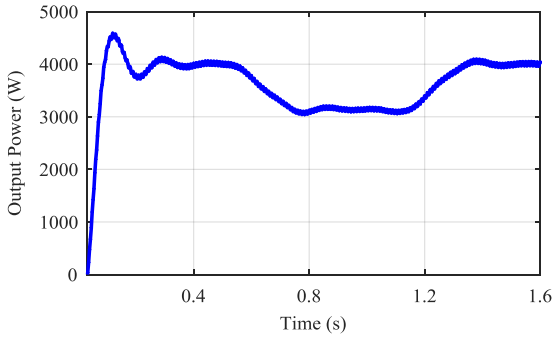

Figure 25. Grid output power

Factors such as large load switching, a short circuit error, driving large loads out of the circuit, etc., cause the network voltage to fluctuate. In Figure 26, the grid voltage decreases by 20% over a [0.5, 0.8] period. Fig 26(b) illustrates that the injected current maintains its sinusoidal shape during voltage reduction and does not phase differ from the voltage. Further, since the solar array injected power has not changed during this period, the size of the injected current has increased in proportion to the decrease in grid voltage.

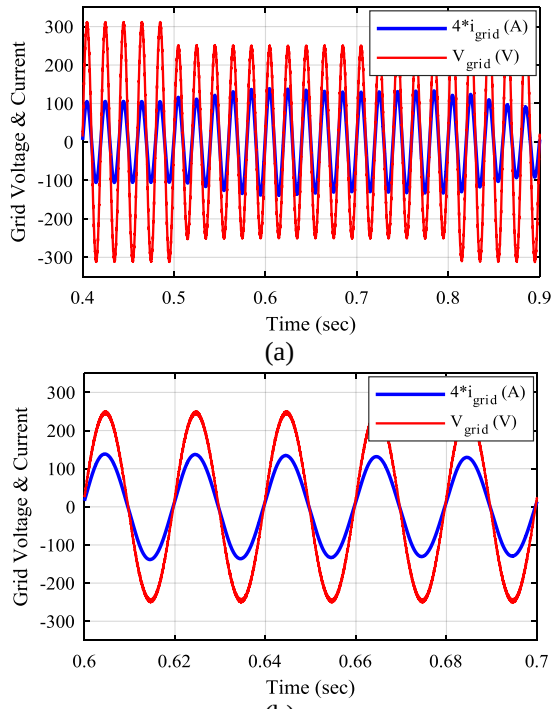

Figure 26. (a) Grid voltage and current waveforms in case of a 20% drop in grid voltage, (b) grid voltage and current waveform within [0.6, 0.7] time interval

Figure 27 demonstrates the grids voltage and current when the grids voltage has increased by 10% within [0.5, 0.8]. In Figure 27(b), the voltage increases between the time intervals [0.6, 0.7]. In the case of increasing the network voltage, similar to decreasing the network voltage, the injected current waveform is sinusoidal, and there is no phase difference with the grid voltage. In addition, due to the increase in network voltage and since the solar array injection power has not changed during this period, the size of the injected current has decreased in proportion to the increase in network voltage. According to the results obtained from Figures 26 and 27, it is clear that the control system used in this paper maintains its stability against the changes in the grid voltage.

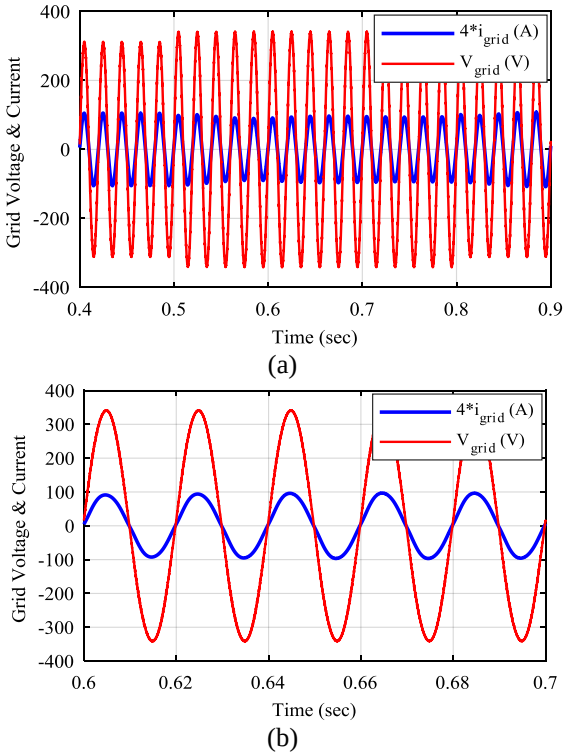

Figure 27. (a) Grid voltage and current waveforms in case of a 10% increase in grid voltage, (b) grid voltage and current waveform within [0.6, 0.7] time interval

At the end, a comparison between the proposed method and the methods that have recently been proposed in the field of improving the performance of the grid-connected inverter control system is presented in Table 5. The references included in this table were evaluated based on their THD of the injected current into the grid, considering the

Table 5. Comparison of the proposed control scheme with other methods

	[39]	[40]	[41]	[42]	[43]	Proposed control scheme
Control method	Capacitor voltage feedback	LMI-LQR current control	Jaya	Grid side current feedback	Quasi-Predictive current control	Positive virtual impedance shaping
Grid side current THD	3.47%	2.43%	2.8%	4.82%	2.15%	1.76%

assumed conditions of each reference. By using the proposed method, it is evident that the current injected into the grid has a higher quality and a lower THD than others.

7. Conclusion

To dampen the resonance caused by the LCL filter in a grid-connected PV power conditioning system, a capacitor-current proportional-integral positive active damping method is proposed. The proposed method extends the frequency range of positive equivalent resistance up to Nyquist frequency, i.e., the full controllable frequency range, and eliminates the non-minimum phase behavior caused by negative resistance, which leads to improved system stability. The proposed damping method uses the equivalent virtual impedance of the grid-connected PV power conditioning system to increase the stability and robustness of the system. To validate the effectiveness of the proposed method, several scenarios have been examined, and a comprehensive evaluation has been conducted. Simulation results indicate that the proposed method for LCL filter resonance dampening in grid-connected PV power conditioning system increases the stability of the grid-tied inverter and results in the injection of high-quality and low THD current into the grid. As a future work, this paper suggests incorporating grid voltage feedforward into the control diagram to enhance the stability of the system under changes in network impedance.

Nomenclature

AD	Active damping
CCF	Capacitor current feedback
V_g	Grid's voltage
PCC	Point of common coupling
i_{L2}	Injected current to the grid
PLL	Phase locked loop
Gi(s)	Current regulator
i_C	Capacitor current
H_{i1}	i_C gain
H_{i2}	i_{L2} gain
K_{PWM}	Inverter transfer function
V_{tri}	Peak of the triangular carrier amplitude
V_{inv}	Peak of the AC voltage generated by the inverter
T_s	Sampling period
K_p	Proportional gain
K_r	Resonant gain
ω_0	Fundamental angular frequency
ω_i	Bandwidth of the resonance
ω_r	LCL angular resonance frequency
RHP	Right half plane
P	Number of RHP poles of the open loop transfer function
Z	Number of RHP poles of the closed loop transfer function
f_{res}	Resonance frequency
f_{sam}	Sampling frequency

References

[1] Navesi, R. B., Nazarpour, D., Ghanizadeh, R., & Alemi, P. (2021). Switchable capacitor bank coordination and dynamic network reconfiguration for improving operation of distribution network integrated with renewable energy resources. *Journal of modern power systems and clean energy*, *10*(3), 637-646.

[2] Srivastava, A., & Seshadrinath, J. (2022). A New Nine Level Highly Efficient Boost Inverter for Transformerless Grid Connected PV Application. *IEEE Journal of Emerging and Selected Topics in Power Electronics*.

[3] Manoharan, P., Subramaniam, U., Babu, T. S., Padmanaban, S., Holm-Nielsen, J. B., Mitolo, M., &

Ravichandran, S. (2020). Improved perturb and observation maximum power point tracking technique for solar photovoltaic power generation systems. *IEEE Systems Journal*, 15(2), 3024-3035.

[4] Bhattacharyya, S., Samanta, S., & Mishra, S. (2020). Steady output and fast tracking MPPT (SOFT-MPPT) for P&O and InC algorithms. *IEEE Transactions on Sustainable Energy*, 12(1), 293-302.

[5] Rasekh, N., & Hosseinpour, M. (2020). Adequate tuning of LCL filter for robust performance of converter side current feedback control of grid connected modified–Y-source inverter. *International Journal of Industrial Electronics Control and Optimization*, 3(3), 365-378.

[6] Huang, M., Zhang, Z., Wu, W., & Yao, Z. (2022). An improved three-level cascaded control for LCL-filtered grid-connected inverter in complex grid impedance condition. *IEEE Access*, *10*, 65485-65495.

[7] Bonaldo, J. P., de Arimatéia Olímpio Filho, J., dos Santos Alonso, A. M., Paredes, H. K. M., & Marafão, F. P. (2021). Modeling and control of a single-phase grid-connected inverter with lcl filter. *IEEE Latin America Transactions*, *19*(02), 250-259.

[8] Mazaheri, A., Barati, F., & Jamil, M. (2019). A Simulation-Aided LCL Filter Design for Grid-Interactive Three-Phase Photovoltaic Inverters. Journal of Solar Energy Research, 4(4), 229-236.

[9] Ding, X., Xue, R., Zheng, T., Kong, F., & Chen, Y. (2022). Robust Delay Compensation Strategy for LCL-Type Grid-Connected Inverter in Weak Grid. *IEEE Access*, *10*, 67639-67652.

[10] Nazib, A. A., Holmes, D. G., & McGrath, B. P. (2021). Self-synchronizing stationary frame inverter-current-feedback control for LCL grid-connected inverters. *IEEE Journal of Emerging and Selected Topics in Power Electronics*, *10*(2), 1434-1446.

[11] Khan, D., Zhu, K., Hu, P., Waseem, M., Ahmed, E. M., & Lin, Z. (2023). Active damping of LCL-Filtered Grid-Connected inverter based on parallel feedforward compensation strategy. *Ain Shams Engineering Journal*, *14*(3), 101902.

[12] Hosseinpour, M., & Rasekh, N. (2019). A single-phase grid-tied PV based trans-z-source inverter utilizing LCL filter and grid side current active damping. *Journal of Energy Management and Technology*, 3(3), 67-77.

[13] Yao, W., Yang, Y., Zhang, X., Blaabjerg, F., & Loh, P. C. (2017). Design and analysis of robust active damping for LCL filters using digital notch filters. *IEEE Transactions on Power Electronics*, 32(3), 2360-2375.

[14] Kouchaki, A., & Nymand, M. (2018). Analytical design of passive LCL filter for three-phase two-level power factor correction rectifiers. *IEEE Transactions on power electronics*, 33(4), 3012-3022.

[15] Bao, C., Ruan, X., Wang, X., Li, W., Pan, D., & Weng, K. (2014). Step-by-step controller design for LCL-type grid-connected inverter with capacitor–current-feedback active-damping. *IEEE Transactions on Power Electronics*, 29(3), 1239-1253.

[16] Xin, Z., Loh, P. C., Wang, X., Blaabjerg, F., & Tang, Y. (2016). Highly accurate derivatives for LCL-filtered grid converter with capacitor voltage active damping. *IEEE Transactions on Power Electronics*, 31(5), 3612-3625.

[17] Huang, M., Wang, X., Loh, P. C., & Blaabjerg, F. (2015). Active damping of LLCL-filter resonance based on LC-trap voltage or current feedback. *IEEE Transactions on Power Electronics*, 31(3), 2337-2346.

[18] Yang, X., Wu, G., Meng, Z., Wang, Y., Ji, L., Xue, H., & Bian, X. (2021). An improved capacitor voltage full feedforward control strategy for LCL- type grid- connected inverter based on control delay compensation. IET Power Electronics, 14(15), 2466-2477.

[19] Zhong, G. X., Wang, Z., Zhou, J., Li, J., & Su, Q. (2022). Coordinated control of active disturbance rejection and grid voltage feedforward for grid- connected inverters. IET Power Electronics.

[20] Hosseinpour, M., Kholousi, A., & Poulad, A. (2022). A robust controller design procedure for LCL- type grid- tied proton exchange membrane fuel cell system in harmonics- polluted network. *Energy Science & Engineering*, 10(10), 3798-3818.

[21] He, Y., Wang, X., Ruan, X., Pan, D., & Qin, K. (2021). Hybrid active damping combining capacitor current feedback and point of common coupling voltage feedforward for LCL-type grid-connected inverter. *IEEE Transactions on Power Electronics*, 36(2), 2373-2383.

[22] Li, X., Wu, X., Geng, Y., Yuan, X., Xia, C., & Zhang, X. (2014). Wide damping region for LCL-type grid-connected inverter with an improved capacitor-current-feedback method. *IEEE Transactions on Power Electronics*, 30(9), 5247-5259.

[23] Pan, D., Ruan, X., Bao, C., Li, W., & Wang, X. (2014). Capacitor-current-feedback active damping with reduced computation delay for improving robustness of LCL-type grid-connected inverter. *IEEE Transactions on Power Electronics*, 29(7), 3414-3427.

[24] Wang, X., Blaabjerg, F., & Loh, P. C. (2016). Grid-current-feedback active damping for LCL resonance in grid-connected voltage-source converters. *IEEE Transactions on Power Electronics*, 31(1), 213-223.
[25] Wang, X., Blaabjerg, F., & Loh, P. C. (2015). Virtual RC damping of LCL-filtered voltage source converters with extended selective harmonic compensation. *IEEE Transactions on Power Electronics*, 30(9), 4726-4737.
[26] Li, X., Wu, X., Geng, Y., Yuan, X., Xia, C., & Zhang, X. (2015). Wide damping region for LCL-type grid-connected inverter with an improved capacitor-current-feedback method. *IEEE Transactions on Power Electronics*, 30(9), 5247-5259.
[27] Chen, C., Xiong, J., Wan, Z., Lei, J., & Zhang, K. (2017). A time delay compensation method based on area equivalence for active damping of an LCL-type converter. *IEEE Transactions on Power Electronics*, 32(1), 762-772.
[28] Pan, D., Ruan, X., Bao, C., Li, W., & Wang, X. (2015). Optimized controller design for LCL-type grid-connected inverter to achieve high robustness against grid-impedance variation. *IEEE Transactions on Industrial Electronics*, 62(3), 1537-1547.
[29] Huang, Q., & Rajashekara, K. (2017, March). Virtual RLC active damping for grid-connected inverters with LCL filters. In *2017 IEEE Applied Power Electronics Conference and Exposition (APEC)* (pp. 424-429).
[30] Zhao, T., Li, J., & Gao, N. (2022). Capacitor-Current-Feedback With Improved Delay Compensation for LCL-Type Grid-Connected Inverter to Achieve High Robustness in Weak Grid. *IEEE Access*, *10*, 127956-127968.
[31] Hosseinpour, M., Asad, M., & Rasekh, N. (2021). A Step-by-Step Design Procedure of a Robust Control Design for Grid-Connected Inverter by LCL Filter in a Weak and Harmonically Distorted Grid. *Iranian Journal of Science and Technology, Transactions of Electrical Engineering*, 45(3), 843-859.
[32] Rasekh, N., Hosseinpour, M., Dejamkhooy, A., & Akbarimajd, A. (2021). Robust power conditioning system based on LCL-type quasi-Y-source inverter for grid connection of photovoltaic arrays. *International Journal of Automation and Control*, 15(6), 692-709.
[33] Li, X., Fang, J., Tang, Y., Wu, X., & Geng, Y. (2018). Capacitor-voltage feedforward with full delay compensation to improve weak grids adaptability of LCL-filtered grid-connected converters for distributed generation systems. *IEEE Transactions on Power Electronics*, 33(1), 749-764.
[34] J Yin, J., Duan, S., & Liu, B. (2013). Stability analysis of grid-connected inverter with LCL filter adopting a digital single-loop controller with inherent damping characteristic. *IEEE Transactions on Industrial Informatics*, 9(2), 1104-1112.
[35] Holmes, D. G., Lipo, T. A., Mcgrath, B. P., & Kong, W. Y. (2009). Optimized design of stationary frame three phase AC current regulators. *IEEE transactions on power electronics*, 24(11), 2417-2426.
[36] Pan, D., Ruan, X., Wang, X., Yu, H., & Xing, Z. (2017). Analysis and design of current control schemes for LCL-type grid-connected inverter based on a general mathematical model. IEEE Transactions on Power Electronics, 32(6), 4395-4410.
[37] Anowar, M. H., & Roy, P. (2019, February). A modified incremental conductance based photovoltaic MPPT charge controller. In *2019 International Conference on Electrical, Computer and Communication Engineering (ECCE)* (pp. 1-5).
[38] Saidi, A., & Benachaiba, C. (2016, November). Comparison of IC and P&O algorithms in MPPT for grid connected PV module. In *2016 8th International Conference on Modelling, Identification and Control (ICMIC)* (pp. 213-218).
[39] Faiz, M. T., Khan, M. M., Jianming, X., Ali, M., Habib, S., Hashmi, K., & Tang, H. (2019). Capacitor voltage damping based on parallel feedforward compensation method for lcl-filter grid-connected inverter. *IEEE Transactions on Industry Applications*, *56*(1), 837-849.
[40] Bimarta, R., & Kim, K. H. (2020). A robust frequency-adaptive current control of a grid-connected inverter based on LMI-LQR under polytopic uncertainties. *IEEE Access*, *8*, 28756-28773.
[41] Padmanaban, S., Priyadarshi, N., Bhaskar, M. S., Holm-Nielsen, J. B., Hossain, E., & Azam, F. (2019). A hybrid photovoltaic-fuel cell for grid integration with jaya-based maximum power point tracking: experimental performance evaluation. *IEEE Access*, *7*, 82978-82990.
[42] Kim, Y. J., & Kim, H. (2019). Optimal design of LCL filter in grid- connected inverters. *IET Power Electronics*, *12*(7), 1774-1782.
[43] Dragičević, T., Zheng, C., Rodriguez, J., & Blaabjerg, F. (2019). Robust quasi-predictive control of $ LCL $-filtered grid converters. *IEEE Transactions on Power Electronics*, *35*(2), 1934-1946.